

Effects of Stellar X-ray Photoevaporation on Planetesimal Formation via the Streaming Instability

Xuchu Ying¹, Beibei Liu^{1, *}, Haifeng Yang¹, Joanna Drażkowska², Sebastian M. Stammler³, Zhaohuan Zhu⁴, Linn E.J. Eriksson⁵, Hongping Deng⁶, Bin Liu¹, and Ping Chen¹

¹ Institute for Astronomy, School of Physics, Zhejiang University, Hangzhou 310058, China
e-mail: xcying@zju.edu.cn

² Max Planck Institute for Solar System Research, Justus-von-Liebig-Weg 3, 37077 Göttingen, Germany

³ University Observatory, Faculty of Physics, Ludwig-Maximilians-Universität München, Scheinerstr. 1, 81679 Munich, Germany

⁴ Department of Physics and Astronomy, University of Nevada, 4505 South Maryland Parkway, Las Vegas, NV 89154, USA

⁵ Department of Astrophysics, American Museum of Natural History, 200 Central Park West, New York, NY 10024, USA

⁶ Shanghai Astronomical Observatory, Chinese Academy of Sciences, Nandan Rd 80th, Shanghai 200030, China

xx.xx.xx; yy.yy.yy

ABSTRACT

Context. The formation of planetesimals via the streaming instability (SI) is a crucial step in planet formation, yet its triggering conditions and efficiency are highly sensitive to both disk properties and specific evolutionary processes.

Aims. We aim to study the planetesimal formation via the SI, driven by the stellar X-ray photoevaporation during the late stages of disk dispersal, and quantify its dependence on key disk and stellar parameters.

Methods. We use the DustPy code to simulate the dust dynamics including coagulation, fragmentation, and radial drift in a viscously accreting disk undergoing stellar X-ray photoevaporation.

Results. Stellar X-rays drive the disk dispersal, opening a cavity at a few au orbital distance and inducing the formation of an associated local pressure maximum. This pressure maximum acts as a trap for radially drifting dust, therefore enhancing the dust density to the critical level required to initiate the streaming instability and the subsequent collapse into planetesimals. The fiducial model produces $31.4 M_{\oplus}$ of planetesimals with an initial dust to final planetesimal conversion efficiency of 20.4%. This pathway is most efficient in larger disks with higher metallicities, lower viscosities, higher dust fragmentation threshold velocities, and/or around stars with higher X-ray luminosities.

Conclusions. This work demonstrates that stellar X-ray photoevaporation is a robust and feasible mechanism for triggering planetesimal formation via the SI during the final clearing phase of protoplanetary disk evolution.

Key words. protoplanetary disks – photoevaporation – streaming instability – planetesimal formation

1. Introduction

Planet formation remains one of the most challenging problems in modern astrophysics (Safronov 1972; Lissauer 1993; Pollack et al. 1996). Over the past three decades, exoplanet surveys using radial velocity, transit, microlensing, and direct imaging techniques have demonstrated that planetary systems are a common outcome of star formation, with the population of detected planets spanning a wide range of masses and orbital architectures (Mayor 2011; Batalha et al. 2013; Cassan et al. 2012; Mulders et al. 2018; Zhu & Dong 2021). The diversity of these systems—from compact super-Earth chains to distant gas giants—provides crucial constraints on the physics of the protoplanetary disk evolution and planet formation (see reviews of Liu & Ji 2020; Drażkowska et al. 2023).

The core accretion scenario offers a broadly successful framework for linking these observations to the final planetary architectures (Pollack et al. 1996; Ida & Lin 2004; Mordasini et al. 2012; Bitsch et al. 2015; Liu et al. 2019; Liu & Ji 2020; Emsenhuber et al. 2021; Pan et al. 2025). In this picture, micron-sized dust particles coagulate into mm-cm pebbles (Blum & Wurm 2008; Birnstiel et al. 2012; Pinilla et al.

2012; Birnstiel et al. 2016), but further growth is uncertain: laboratory experiments (Blum & Münch 1993; Blum & Wurm 2000, 2008; Güttler et al. 2010), and numerical simulations (Brauer et al. 2008; Zsom et al. 2010; Okuzumi et al. 2012; Kataoka et al. 2013; Drażkowska et al. 2016) all indicate that bouncing, fragmentation, and rapid inward drift prevent pebbles from directly forming kilometer-sized planetesimals. These barriers are most severe inside ice lines or in disks with low dust-to-gas ratios, where pebbles drift inward before significant growth can occur (Drażkowska et al. 2023). The conversion of mm-sized solids into planetesimals therefore remains one of the least understood stages of planet formation (Johansen et al. 2014; Liu & Ji 2020; Drażkowska et al. 2023), demanding an additional, efficient concentration mechanism (Birnstiel et al. 2016; Drażkowska et al. 2016).

The streaming instability (SI) is widely considered a leading candidate for overcoming these barriers (Youdin & Goodman 2005; Johansen et al. 2007; Bai & Stone 2010; Carrera et al. 2015; Li & Youdin 2021; Lim et al. 2024, 2025a,b). By tapping the relative motion between gas and solids, the SI concentrates drifting solids into dense filaments that can collapse gravitationally into planetesimals. Its activation, however, depends sensitively on local dust-to-gas ratio, particles' Stokes

* Corresponding author: bbliu@zju.edu.cn

number, and disk turbulence (Bai & Stone 2010; Yang et al. 2017; Drążkowska et al. 2014; Lim et al. 2024), and local dust-to-gas ratio several times that of the sun is typically required (Johansen et al. 2009b; Carrera et al. 2015; Drążkowska et al. 2016; Liu & Ji 2020). This raises a key question: how and where can protoplanetary disks enhance the dust-to-gas ratio sufficiently to trigger the SI?

High-resolution imaging of protoplanetary disks has revealed ubiquitous substructures—such as rings, gaps, and cavities—which are interpreted as evidences that dust growth and radial drift are already actively reshaping disks at very young ages (Huang et al. 2018; Dullemond et al. 2018; Andrews 2020). Pressure bumps are thought to be natural sites for halting dust drift and locally boosting the metallicity. They may arise from gap opening by massive planets (Kobayashi et al. 2012; Zhu et al. 2012; Gonzalez et al. 2015; Eriksson et al. 2020), at the inner edges of magnetically inactive dead zones (Varnière & Tagger 2006; Lyra et al. 2009; Dzyurkevich et al. 2010), from zonal flows generated by hydrodynamical or magnetic instabilities (Johansen et al. 2009a; Ditttrich et al. 2013; Bai 2014; Raettig et al. 2015; Xu & Bai 2022; Lehmann & Lin 2025), in the ice line regions (Ida & Guillot 2016; Drążkowska & Alibert 2017; Schoonenberg & Ormel 2017), or at the outer edges of photoevaporative cavities (Carrera et al. 2017; Ercolano et al. 2017).

High-energy radiation, particularly X-rays from young stellar hosts, plays a critical role in clearing gas from protoplanetary disks during their late evolutionary stages (Owen et al. 2010, 2012; Ercolano et al. 2017; Wang & Goodman 2017; Jennings et al. 2018; Picogna et al. 2019). This radiation heats and ionizes the upper layers of the disk, driving the photoevaporative winds that steadily deplete the gas. This process initially opens a cavity at a few au orbital distance for a solar-mass star (closer-in for a lower-mass star). As depletion continues, the cavity expands outward (Owen et al. 2010; Alexander et al. 2014; Ercolano & Pascucci 2017; Picogna et al. 2019). A local pressure maximum forms near the expanding cavity’s edge, which efficiently traps drifting dust (Pinilla et al. 2018; Gárate et al. 2021, 2023). This evolving pressure bump can enhance the local metallicity and trigger the SI, potentially facilitating late-stage planetesimal formation (Carrera et al. 2017; Ercolano et al. 2017). Similarly, Throop & Bally (2005) pointed out that the external photoevaporation from the nearby massive stars removes the gas efficiently, while the dust population remains largely unaffected. This can also increase the disk dust-to-gas ratio.

This paper investigates whether stellar X-ray photoevaporation can produce the conditions required to trigger the SI and form planetesimals. We employ the `DustPy` code to couple models of viscous gas evolution with dust coagulation, fragmentation, and radial drift, explicitly including photoevaporation to simulate the formation and inside-out movement of a disk cavity with its associated pressure bumps. By applying established SI criteria to these evolving disks, we determine the circumstances under which the photoevaporation-driven dispersal promotes the planetesimal formation.

Our paper is organized as follows. The model is introduced in Sect. 2. Our main results and parameter exploration are presented in Sect. 3. The implications and uncertainties are discussed in Sect. 4. The conclusions are drawn in Sect. 5.

2. Method

In this section, we introduce the basics of our model. The prescriptions of disk evolution, stellar X-ray photoevaporation, and planetesimal formation are described in Sect. 2.1, 2.2 and Sect. 2.3, respectively, whereas the simulation setup is given in Sect. 2.4.

2.1. Disk model

2.1.1. Gas component

The initial gas disk surface density is adopted from the self-similar solution of Lynden-Bell & Pringle (1974)

$$\Sigma_{g0} = \frac{M_{\text{disk}}}{2\pi R_c^2} \left(\frac{r}{R_c} \right)^{-1} \exp \left(-\frac{r}{R_c} \right), \quad (1)$$

where M_{disk} is the onset gas disk mass, R_c is the disk characteristic radius, and r is the radial distance from the central star.

Considering a passively irradiated disk with a constant irradiation angle of $\theta=0.05$, the disk midplane temperature can be written as

$$T = \left(\frac{\theta L_{\star}}{8\pi r^2 \sigma_{\text{SB}}} \right)^{1/4} = 220 \text{ K} \left(\frac{r}{\text{au}} \right)^{-1/2}, \quad (2)$$

where $L_{\star}=4\pi\sigma_{\text{SB}}R_{\star}^2T_{\text{eff}}^4$ is the stellar luminosity, and σ_{SB} is the Stefan-Boltzmann constant. We choose a premain-sequence solar-mass central star with a stellar radius of $R_{\star}=2R_{\odot}$ and an effective temperature of $T_{\text{eff}}=5772$ K.

The aspect ratio of the gas disk is therefore expressed as

$$h_g = \frac{c_s}{v_K} = \frac{H_g}{r} = 0.03 \left(\frac{r}{\text{au}} \right)^{1/4}, \quad (3)$$

where c_s is the isothermal gas sound speed, $v_K=\sqrt{GM_{\star}/r}$ is the Keplerian velocity, G is the gravitational constant, M_{\star} is the stellar mass, and H_g is the gas disk scale height.

The gas pressure gradient parameter is defined as

$$\eta = -\frac{h_g^2}{2} \frac{\partial \ln P_g}{\partial \ln r}, \quad (4)$$

where P_g is the midplane gas pressure. Another useful dimensionless parameter that quantifies the gas pressure effect can be defined as

$$\Pi = \frac{\eta v_K}{c_s}, \quad (5)$$

where ηv_K is the gas headwind velocity, indicating how much the azimuthal velocity of the gas deviates from the local Keplerian velocity.

The gas surface density is evolved through the viscous advection-diffusion equation (Lynden-Bell & Pringle 1974),

$$\frac{\partial}{\partial t} \Sigma_g + \frac{1}{r} \frac{\partial}{\partial r} (r \Sigma_g v_g) = \dot{\Sigma}_{\text{PE},g}, \quad (6)$$

where v_g is the radial gas velocity and the sink term $\dot{\Sigma}_{\text{PE},g}$ is the gas surface density decay rate driven by the stellar X-ray radiation, the prescription of which will be presented in Sect. 2.2.

The radial viscous velocity of the gas reads

$$v_g = -\frac{3}{\Sigma_g} \frac{\partial}{\partial r} (\Sigma_g v \sqrt{r}), \quad (7)$$

where $v=\alpha c_s H_g$ is the gas turbulent viscosity, and α is the dimensionless viscous parameter (Shakura & Sunyaev 1973).

2.1.2. Dust transport

The advection-diffusion equation for the dust is given by Clarke & Pringle (1988)

$$\frac{\partial}{\partial t} \Sigma_d + \frac{1}{r} \frac{\partial}{\partial r} \left[r \Sigma_d v_d - r D_d \Sigma_g \frac{\partial}{\partial r} \left(\frac{\Sigma_d}{\Sigma_g} \right) \right] = \dot{\Sigma}_{\text{PE},d} + \dot{\Sigma}_{\text{plt}}, \quad (8)$$

where Σ_d and v_d are the surface density and radial velocity of dust, $\dot{\Sigma}_{\text{PE},d}$ and $\dot{\Sigma}_{\text{plt}}$ are the dust mass-loss rates driven by the stellar X-ray photoevaporation and planetesimal formation, respectively. Since the dust coagulation is considered, in practical, the above transport equation is solved for dust with different mass bins. The disk metallicity is defined as $Z = \Sigma_d / \Sigma_g$.

The dust diffusivity taken from Youdin & Lithwick (2007) reads

$$D_d = \frac{D_g}{1 + \text{St}^2} = \frac{\delta_r c_s H_g}{1 + \text{St}^2}, \quad (9)$$

where $D_g = \delta_r c_s H_g$ is the gas diffusivity and the dimensionless turbulent parameter δ_r represents the turbulent diffusion in the radial direction. We set $D_d = 0$ for most of our simulations. Including the dust diffusivity has a negligible effect on our results, since the timescale for dust to diffuse across its trapping region is much longer than that of planetesimal formation (see discussions in Sect. 4.2).

The aerodynamic size of the dust particles can be quantified by their Stokes number (Whipple 1972, 1973; Weidenschilling 1977),

$$\text{St} = \begin{cases} \frac{\pi}{2} \frac{a_d \rho_{\bullet}}{\Sigma_g} & \text{at } a_d \leq \frac{9}{4} \lambda_{\text{mfp}}, \\ \frac{2\pi}{9} \frac{a_d^2 \rho_{\bullet}}{\lambda_{\text{mfp}} \Sigma_g} & \text{at } a_d > \frac{9}{4} \lambda_{\text{mfp}}. \end{cases} \quad (10)$$

Here a_d is the particle's physical size, λ_{mfp} is the mean free path of disk gas, and ρ_{\bullet} is the particle's internal density, chosen to be 1.67 g cm^{-3} as the default value.

The radial dust velocity is given by

$$v_d = \frac{v_g + 2v_{\text{drift,max}} \text{St}}{1 + \text{St}^2}, \quad (11)$$

with the maximum drift velocity $v_{\text{drift,max}} = -\eta v_K$.

2.1.3. Dust coagulation

In our simulations, the dust coagulation is calculated by solving the Smoluchowski equation (Smoluchowski 1916; Stammler & Birnstiel 2022). Basically, the dust initially grows through pair-wise collisions until reaching the radial drift barrier or the fragmentation barrier.

Although our simulations employ the DustPy code (Stammler & Birnstiel 2022), which directly solves the full Smoluchowski equation, we briefly introduce the concepts of the fragmentation and drift barriers to provide physical intuition for the dust growth process. These barriers describe the limiting regimes in which dust growth is halted by either fragmentation or radial drift, and they are commonly used to interpret the size limits of dust in protoplanetary disks.

The dust growth, fragmentation, and radial drift have been investigated in-depth (Safronov 1972; Weidenschilling 1977, 1980; Nakagawa et al. 1986; Dominik & Tielens 1997; Brauer et al. 2008; Blum & Wurm 2008; Birnstiel et al. 2012). Assuming that the relative velocity between dust is driven

by disk turbulence $v_{\text{rel}} \approx \sqrt{3\delta_r \text{St}} c_s$ (Ormel & Cuzzi 2007), the growth timescale taken from Birnstiel et al. (2012) reads

$$\tau_{\text{growth}} = \frac{a_d}{\dot{a}_d} = \frac{\rho_{\bullet} a_d}{\rho_d v_{\text{rel}}} \approx \frac{1}{Z \Omega_K}, \quad (12)$$

where ρ_d is the dust volume density, and $\Omega_K = v_K / r$ is the Keplerian frequency. The dust radial drift timescale adopted from Birnstiel et al. (2012) reads

$$\tau_{\text{drift}} = \frac{r}{v_d} \approx \frac{1}{\eta \text{St} \Omega_K}. \quad (13)$$

When the drift timescale is shorter than the growth timescale, the in-situ growth cannot proceed. By equating these two timescales, one can derive the particles' Stokes number in the radial drift barrier as

$$\text{St}_{\text{drift}} = \frac{Z}{2\eta}. \quad (14)$$

On the other hand, when the dust particles' relative velocities exceed a specific threshold, they will fragment during collisions rather than perfectly merge. This sets another limit on the size of the particles, referred to as the fragmentation barrier. The fragmentation barrier in the turbulent velocity driven regime is given by

$$\text{St}_{\text{frag}} = \frac{v_{\text{frag}}^2}{3\delta_t c_s^2}, \quad (15)$$

where v_{frag} is the fragmentation threshold velocity and δ_t is the turbulent mixing parameter. In reality, the Stokes number of the largest particles can be approximated as $\text{St} = \min(\text{St}_{\text{frag}}, \text{St}_{\text{drift}})$.

It is worth noting that the turbulent mixing parameters are defined in three forms: δ_r , δ_t , and δ_z . For MRI-driven disk turbulence, which is approximately isotropic, angular momentum transport is roughly equivalent to mass diffusion (Johansen & Klahr 2005; Zhu et al. 2012; Zhou et al. 2022) ($v \approx D_g$), so that $\delta_r \approx \delta_t \approx \delta_z \approx \alpha$. In our default models, we set $\delta_r = 0$, $\delta_t \approx \delta_z \approx \alpha$, and explore the influences of these parameters in Sect. 4.2.

2.2. Stellar X-ray photoevaporation

Intense X-ray radiation from the young, active central star heats the upper layers of the disk, inducing the hot gas and dust to escape as a photoevaporative wind (Alexander et al. 2014; Ercolano & Pascucci 2017). In this work we focus on the stellar X-ray radiation, the influence of which is incorporated as the sink terms in Eq. 6 and Eq. 8.

We adopt the normalized $\dot{\Sigma}_{\text{PE},g}$ profiles from Owen et al. (2012) for primordial disks and disks with inner holes. We also note that alternative prescriptions, such as that of Picogna et al. (2019), yield different radial mass-loss distributions due to differences in their hydrodynamic setups and thermochemical treatments. More recently, Sellek et al. (2024) find that the Owen et al. (2012)'s prescription remain in good agreement with their radiation-hydrodynamic simulations. This provides the motivation for our choice of the Owen et al. (2012) photoevaporation prescription in this work. Although these prescriptions differ in their detailed radial mass-loss profiles, a systematic exploration of how these differences may impact the disk dispersal and dust dynamics is beyond the scope of this study.

Owen et al. (2012) calculated the $\dot{\Sigma}_{\text{PE,g}}$ profiles for both primordial disks and disks with inner holes, based on their radiation-hydrodynamical model.

$$\dot{M}_{\text{PE}} = \begin{cases} 1.65 \times 10^{-8} \left(\frac{M_{\star}}{M_{\odot}}\right)^{-0.068} \\ \times \left(\frac{L_{\text{X}}}{L_{\text{X},\odot}}\right)^{1.14} M_{\odot} \text{ yr}^{-1} & [\text{primordial disk}], \\ 1.27 \times 10^{-8} \left(\frac{M_{\star}}{M_{\odot}}\right)^{-0.148} \\ \times \left(\frac{L_{\text{X}}}{L_{\text{X},\odot}}\right)^{1.14} M_{\odot} \text{ yr}^{-1} & [\text{disk with inner hole,} \\ & \text{at } r > r_{\text{hole}}]. \end{cases} \quad (16)$$

The typical X-ray luminosity of a solar-mass T Tauri star can be expressed as $L_{\text{X},\odot} = 2.34 \times 10^{30} \text{ erg s}^{-1}$ (Preibisch et al. 2005). Taking into account the correlation between X-ray luminosity of T Tauri stars and stellar mass (see Sect. 4.2 in Preibisch et al. 2005), the integrated gas mass-loss rate driven by the stellar X-ray photoevaporation can be written as

$$\dot{M}_{\text{PE}} = \begin{cases} 1.65 \times 10^{-8} \left(\frac{M_{\star}}{M_{\odot}}\right)^{1.57} M_{\odot} \text{ yr}^{-1} & [\text{primordial disk}], \\ 1.27 \times 10^{-8} \left(\frac{M_{\star}}{M_{\odot}}\right)^{1.49} M_{\odot} \text{ yr}^{-1} & [\text{disk with inner hole,} \\ & \text{at } r > r_{\text{hole}}]. \end{cases} \quad (17)$$

For the primordial disks, the photoevaporative mass-loss rate $\dot{\Sigma}_{\text{PE,g}}$ peaks at $\sim 2\text{--}3$ au. After the cavity forms, we set the gas depletion rate at $r < r_{\text{hole}}$ to a constant to ensure rapid gas removal there. Since the inner disk does not participate in planetesimal formation, this treatment does not alter the final mass of planetesimals. We adopt a relatively high X-ray luminosity $L_{\text{X}} = 6.15 \times 10^{30} \text{ erg s}^{-1} = 2.6 L_{\text{X},\odot}$ in our default model, and assume that L_{X} remains constant during the short disk dispersal phase. Our simulations are designed to follow the final dispersal of the disk. Choosing a higher L_{X} , corresponding to a more X-ray-active young star (see Fig. 3 in Preibisch et al. 2005), allows the photoevaporation-driven clearing phase to complete within ~ 1 Myr.

The stellar photoevaporation also influences the dust dynamics. Following Facchini et al. (2016) and Sellek et al. (2020), we assume that particles smaller than the entrained size, a_{ent} , can be blown away by the wind, where

$$a_{\text{ent}} = \frac{v_{\text{th}} \dot{M}_{\text{PE}}}{4\pi \mathcal{F} \rho_{\bullet} G M_{\star}}, \quad (18)$$

where $v_{\text{th}} = \sqrt{8/\pi} c_{\text{s}}$ is the thermal velocity of the gas and $\mathcal{F} = H_{\text{g}} / \sqrt{r^2 + H_{\text{g}}^2}$ corresponds to the disk geometric factor. For particles smaller than the entrained size a_{ent} , we set the dust mass-loss rate

$$\dot{\Sigma}_{\text{PE,d}}^i = f_{\text{ent}} \cdot Z^i \cdot \dot{\Sigma}_{\text{PE,g}}, \quad (19)$$

where $\dot{\Sigma}_{\text{PE,d}}^i$ is the dust mass-loss rate driven by the stellar X-ray photoevaporation within a specific dust mass bin i , f_{ent} is the entrained mass fraction, and Z^i is the metallicity for that mass bin. Following Sellek et al. (2020), we set $f_{\text{ent}} = 1$ in our simulations.

2.3. Streaming instability criterion and planetesimal formation

Several literature studies have investigated the critical condition for triggering the SI. The classical criterion for the onset of the SI is proposed by Youdin & Goodman (2005) through a linear stability analysis. They found that the SI criterion can be fulfilled when the midplane volume density ratio of dust-to-gas approaches unity. Their result laid the foundation for subsequent theoretical and numerical studies. Carrera et al. (2015) explored this issue by performing 2D numerical simulations and obtained the metallicity threshold Z_{crit} as a function of particles' Stokes number. Later Yang et al. (2017) reduced this clumping threshold with an improved numerical method. Li & Youdin (2021) further quantified how $Z_{\text{crit}}(\text{St})$ vary with simulation setups. They found that sub-solar metallicity can already induce the dust clumping at $\text{St} \sim 0.1\text{--}1$, lower than previous results. However, their numerically study is only 2D and without taking into account of disk turbulence. More recently, Lim et al. (2024) advanced the understanding of the SI condition by performing 3D stratified shearing box simulations that include both particles' self-gravity and externally forced turbulence. Their work provides a more accurate threshold for evaluating the planetesimal formation in global disk models.

For the purpose of generality, here we list three SI criteria, ranging from the early linear analysis of Youdin & Goodman (2005) to the most updated numerical simulations of Lim et al. (2024). The influence of adopting different SI criteria on our study will be discussed in Sect. 3.1.

To the zero order, the analytical SI criterion can be expressed as the midplane volume density ratio of dust-to-gas, where

$$\epsilon_{\text{crit}} \equiv \rho_{\text{d}} / \rho_{\text{g}} = 1. \quad (20)$$

By explicitly quantifying how turbulence affects the SI-induced clumping, the new derived criteria from Lim et al. (2024) bridge the gap between idealized SI theory and turbulent disk environments. The ϵ_{crit} criterion provided by Lim et al. (2024) reads

$$\log_{10} \epsilon_{\text{crit}} = 0.42(\log_{10} \text{St})^2 + 0.72(\log_{10} \text{St}) + 0.37. \quad (21)$$

Meanwhile, Lim et al. (2024) also provided the Z_{crit} criterion such that

$$\log_{10} Z_{\text{crit}} = 0.15(\log_{10} \delta_{\text{t}})^2 - 0.24(\log_{10} \text{St} \log_{10} \delta_{\text{t}}) - 1.48(\log_{10} \text{St}) + 1.18(\log_{10} \delta_{\text{t}}). \quad (22)$$

The above two criteria hold for particles with $0.01 \leq \text{St} \leq 0.1$ and disk turbulent level of $10^{-4} \leq \delta_{\text{t}} \leq 10^{-3}$. We also use YG05, L24E, and L24Z to represent Eqs. 20, 21, and 22 hereafter.

It is worth noting that L24Z (Eq. 22) is derived at $\Pi = 0.05$. Physically, a more decisive factor that sets the SI clumping should actual be Z/Π in the above equation (Sekiya & Onishi 2018). In our simulations that include the stellar X-ray photoevaporation, however, the Π value varies significantly across the disk and crosses zero at the outer cavity edge. This variability makes it impractical to apply a correction to the criterion directly. We therefore adopt the ϵ_{crit} criterion of L24E (Eq. 21), which shares the same physical basis as the Z_{crit} criterion of L24Z (Eq. 22), and subsequently calculate the midplane density ratio in our 1D code to incorporate the effects of Π . A key advantage of L24E (Eq. 21) is its ability to capture turbulence variations from the SI (specifically through Π) via the self-consistent modification of the dust scale height. The specific method is detailed below.

Table 1: List of simulation and model parameters used in Sect. 3.

| Model | $M_{\text{disk}} [M_{\odot}]$ | $R_c [\text{au}]$ | α | δ_t | Z_0 | $v_{\text{frag}} [\text{m s}^{-1}]$ | $L_X [L_{X,\odot}]$ |
|------------|-------------------------------|-------------------|-----------|------------|-------|-------------------------------------|---------------------|
| run_fid | 0.05 | 60 | 10^{-4} | 10^{-4} | 0.01 | 5.0 | 2.6 |
| run_metal | 0.05 | 60 | 10^{-4} | 10^{-4} | 0.02 | 5.0 | 2.6 |
| run_lumi | 0.05 | 60 | 10^{-4} | 10^{-4} | 0.01 | 5.0 | 1.0 |
| run_alpha | 0.05 | 60 | 10^{-3} | 10^{-4} | 0.01 | 5.0 | 2.6 |
| run_dsize1 | 0.10 | 120 | 10^{-4} | 10^{-4} | 0.01 | 5.0 | 2.6 |
| run_dsize2 | 0.05 | 120 | 10^{-4} | 10^{-4} | 0.01 | 5.0 | 2.6 |
| run_frag | 0.05 | 60 | 10^{-4} | 10^{-4} | 0.01 | 1.0 | 2.6 |

Table 2: Resultant planetesimal masses and dust-to-planetesimal conversion efficiencies.

| Model | $M_{\text{plt}} [M_{\oplus}]$ | | | | | Conversion Efficiency [%] |
|------------|-------------------------------|---------|----------|-----------|-------|---------------------------|
| | 1–3 au | 3–10 au | 10–30 au | 30–100 au | Total | |
| run_fid | 0 | 14.0 | 16.5 | 0.9 | 31.4 | 20.4 |
| run_metal | 0 | 26.2 | 20.7 | 1.3 | 48.2 | 15.3 |
| run_lumi | 0 | 0 | 0.8 | 0.2 | 1.0 | 0.6 |
| run_alpha | 0 | 5.9 | 8.0 | 0.7 | 14.6 | 9.5 |
| run_dsize1 | 0 | 23.7 | 73.8 | 23.5 | 125.0 | 39.7 |
| run_dsize2 | 0 | 9.7 | 23.8 | 28.9 | 62.4 | 40.5 |
| run_frag | 0 | 0 | 0 | 0 | 0 | 0 |

In absence of the SI-induced dust concentration, the dust scale height adopted from Dubrulle et al. (1995) can be written as

$$H_d = H_g \sqrt{\frac{\delta_z}{\delta_z + St}}, \quad (23)$$

where δ_z is the vertical turbulent mixing parameter. SI can act as an additional turbulent source to affect the vertical dust distribution. Taking this into account, Carrera et al. (2025) and Eriksson et al. (2025) derived the effective dust scale height as

$$H_d = H_g \sqrt{\frac{1 + St}{1 + St + \epsilon}} \sqrt{\left(\frac{\Pi}{5}\right)^2 + \frac{\delta_z}{\delta_z + St}}. \quad (24)$$

Our simulation is 1D and only calculates the vertical integrated gas and dust quantities. In order to derive the volume density, the vertical distribution of the dust needs to be intrinsically assumed. Despite that the dust vertical distribution might not be Gaussian-like owing to the SI effect (Lim et al. 2024), we still assume that the dust midplane density approximately follows $\rho_d \propto \Sigma_d / H_d$, and therefore,

$$\epsilon \equiv \frac{\rho_d}{\rho_g} = Z \frac{H_g}{H_d}. \quad (25)$$

Let $\xi \equiv \frac{Z}{\sqrt{1+St} \sqrt{\left(\frac{\Pi}{5}\right)^2 + \frac{\delta_z}{\delta_z + St}}}$, we can obtain

$$\epsilon = \frac{\xi^2 + \sqrt{\xi^4 + 4\xi^2(1 + St)}}{2}. \quad (26)$$

We note that the aforementioned SI criteria are all derived from simulations based on single-size particles (see Bai & Stone 2010; Zhu & Yang 2021 for multi-species). In this study we consider the drift and coagulation of dust particles with a wide size

range. We thus use the mass-weighted mean Stokes number to represent the bulk dust population, the formula of which can be written as

$$St_{\text{mean}} = \frac{\sum_i St^i \cdot \Sigma_d^i}{\sum_i \Sigma_d^i}, \quad (27)$$

where St^i and Σ_d^i are the corresponding particles' Stokes number and mass density in the mass bin i . The Stokes number of the dust population can therefore be specified at any given t and r . We adopt St_{mean} for calculating ϵ_{crit} and H_d .

Once $\epsilon \geq \epsilon_{\text{crit}}$ is satisfied, we transform the dust into planetesimals via

$$\dot{\Sigma}_{\text{plt}} = -\zeta \frac{\Sigma_d}{t_{\text{set}}} = -\zeta \Sigma_d \frac{\Omega_K}{1 + St^{-1}}, \quad (28)$$

where $t_{\text{set}} = [\Omega_K / (1 + St^{-1})]^{-1}$ is the settling time, which corresponds to the timescale on the formation of the SI filaments (Yang et al. 2017). We adopt this formula of t_{set} to eliminate interference of particles with extremely large Stokes number, such as the particles within the inner cavity (see Fig. 1b, Sect. 3.1).

The planetesimal conversion efficiency, ζ , represents the fraction of dust converted into planetesimals per settling time. Numerically, if ζ is too large, the entire dust mass within a radial bin would be depleted within a single timestep, leading to numerical instability. Physically, once the SI condition is met, dust trapped in a pressure bump is expected to rapidly transform into planetesimals within dozens of settling times (t_{set}). Given that t_{set} is significantly shorter than the timescale for the movement of the photoevaporative cavity ($\sim 10^3$ – 10^5 yr), planetesimal formation should be efficient regardless of the adoption of ζ values across a broad parameter range. Based on the simulations of Simon et al. (2016) and following Schoonenberg et al. (2018), we set $\zeta = 0.1$. For completeness, we test several planetesimal formation prescriptions. Our fiducial model adopts the rate modified from Schoonenberg et al. (2018). We further examine

the formulations by Drążkowska et al. (2016), which consider particles with $\text{St} > 0.01$ and an efficiency parameter $\zeta = 0.01$, as well as the smooth transition function introduced by Miller et al. (2021) to determine the local planetesimal formation fraction. The resulting differences in the total planetesimal mass are minor, suggesting that our results are robust against the specific choice of the planetesimal formation formula.

We also note that although the SI criterion of L24E (Eq. 21) is derived for particles with Stokes numbers in the range of ~ 0.01 – 0.1 , in our study the dominated dust population involved in planetesimal formation naturally falls within a similar Stokes number range constrained by the drift and fragmentation barriers. The particles' mean Stokes number (St_{mean}) reaches only approximately a few tenths even during the late stages of disk evolution (see Fig. 1b, Sect. 3.1). Practically, we extrapolate the thresholds beyond their original Stokes number range. We also test this approach and find that the difference is minor when restricting the Stokes number to ~ 0.01 – 0.1 compared to using the full size domain.

2.4. Simulation setup

We adopt the `DustPy` (v1.0.5) code (Stammler & Birnstiel 2022) to study the radial evolution of the gas and the dust in protoplanetary disk, with the effects of viscous gas evolution, stellar X-ray photoevaporation, dust coagulation, fragmentation and radial drift. The radial grid extends from 1–300 au with 256 logarithmically spaced grid cells. We additionally implement the local refinement of the grids in the planetesimal formation region driven by stellar X-ray photoevaporation, spanning 5–20 au in the typical simulation setups. We verify that the final mass of planetesimals converges with this treatment and a higher radial grid resolution. We adopt 120 bins for dust mass, logarithmically from 10^{-12} to 10^5 g. The inner boundary condition for the dust and gas densities is set to be a constant gradient, whereas the outer boundary condition is set to be a floor value.

There are six key parameters in our model: the initial metallicity Z_0 , the stellar X-ray luminosity L_X , the gas viscous parameter α , the initial gas disk mass M_{disk} , the disk characteristic disk radius R_c , and the dust fragmentation threshold velocity v_{frag} . The default parameter values are listed in Table 1.

3. Results

In this section, we describe the results of the fiducial run in Sect. 3.1, and explore different model parameters from Sect. 3.2 to Sect. 3.6. Resultant planetesimal masses and dust-to-planetesimal conversion efficiencies are listed in Table 2, and the radial mass distributions of planetesimals are presented in Fig. 5.

3.1. Fiducial model

For the fiducial run (`run_fid`), we choose initial disk mass $M_{\text{disk}} = 0.05 M_{\odot}$, characteristic disk radius $R_c = 60$ au, viscous parameter $\alpha = 10^{-4}$, initial metallicity $Z_0 = 0.01$, fragmentation threshold velocity $v_{\text{frag}} = 5$ m s $^{-1}$, stellar X-ray luminosity $L_X = 2.6 L_{X,\odot}$. The SI criterion is adopted from L24E (Eq. 21).

Fig. 1a shows the dust and gas disk evolution at different snapshots in `run_fid`. At $t = 0.35$ Myr, an inner cavity opens at around 3 au. The outer edge of this inner cavity expands outward rapidly, reaching ~ 10 au at $t = 0.45$ Myr, and ~ 100 au at $t = 0.90$ Myr, respectively. Due to the dust radial drift and gas

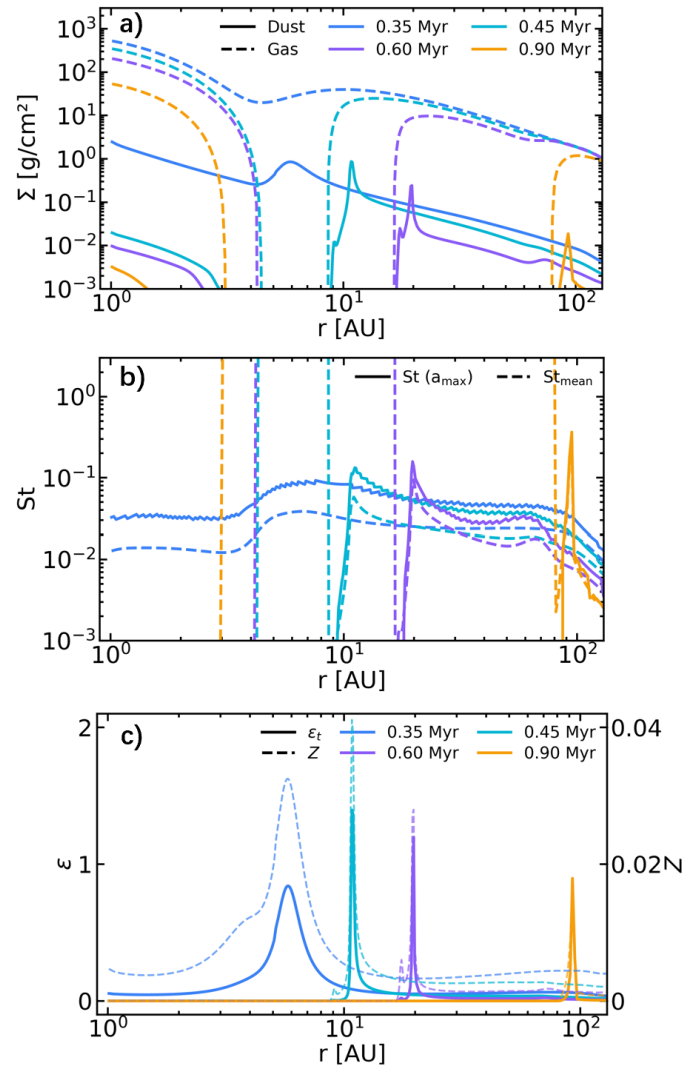


Fig. 1: The time and radial distance evolution of different quantities in the fiducial model. Panel a): Gas (dashed lines) and dust (solid lines) surface density. Panel b): Stokes number of the maximum-size dust particles (solid lines) and the mean Stokes number of the dust particles (dashed lines) at each radial bin. Maximum-size refers to the size of the particle whose surface density is at the peak of the mass bins hereafter. Panel c): Midplane density ratio ϵ (solid lines) and metallicity Z (dashed lines).

disk inside-out clearing, the dust gets accumulated and forms a ring-like structure at the edge of the inner disk cavity.

This can also be clearly seen in Fig. 2, which presents the synthetic dust continuum images at the $880 \mu\text{m}$ wavelength at three different epochs. At the early phase of $t = 0.25$ Myr, the disk is driven by viscous evolution, and the dust is distributed relatively smoothly throughout the disk (see Fig. 2a). Fig. 2b shows the onset of photoevaporation-driven clearing, whereas in Fig. 2c, the inner cavity expands further out, with a strong dust emission at its outer edge. At the cavity's edge, rapid gas clearing yields a local pressure bump, providing a natural site for dust concentration. The images are generated with `RADMC-3D` based on the one-dimensional `DustPy` outputs mapped onto two-dimensional axisymmetric grids. We adopt 38 logarithmically spaced dust-size bins between $5 \mu\text{m}$ and 17 cm , and assume that

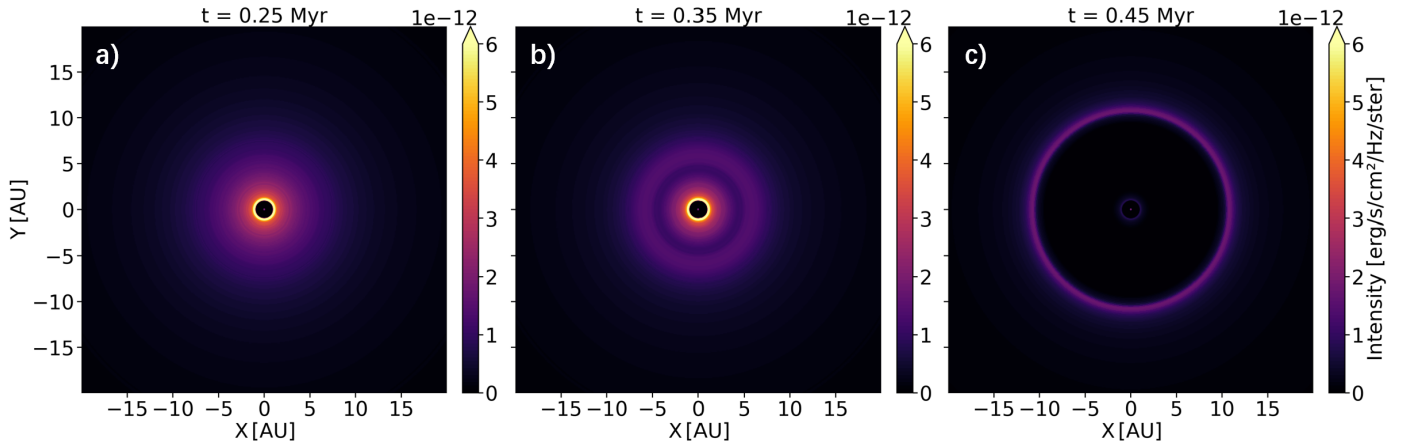


Fig. 2: Synthetic $880\text{ }\mu\text{m}$ continuum images from the fiducial model. Panel a): $t=0.25$ Myr, pre-cavity stage; Panel b): $t=0.35$ Myr, onset of photoevaporative cavity opening; Panel c): $t=0.45$ Myr, post-cavity stage.

the disk is passively heated by stellar irradiation. Dust temperatures are computed using Monte Carlo radiative transfer, and synthetic images are convolved to $880\text{ }\mu\text{m}$, using isotropic scatterings and the DSHARP opacity model (Birnstiel et al. 2018).

Fig. 1b demonstrates the Stokes number of the maximum-size dust particles (solid lines) and the mean Stokes number of the dust population (dashed lines). Overall, the $St(a_{\max})$ and St_{mean} values are higher near the outer edge of cavity than in the residual disk regions. This is because dust drifts slower near the pressure bump, enhancing the local coagulation. We also obtain that St_{mean} near the cavity's edge is ~ 0.05 at $t=0.45$ Myr, ~ 0.1 at $t=0.60$ Myr, and ~ 0.2 at $t=0.90$ Myr. Thus, St_{mean} remains largely below 0.1 within 30 au, which is the most relevant for planetesimal formation. This size is within the range where L24E (Eq. 21) is valid. We also note that the sharp increase in St_{mean} just inside the cavity is caused by the floor values of the surface densities set in DustPy. These anomalous Stokes number values, as discussed in Sect. 2.3, can lead to the artificial formation of planetesimals in dust-depleted regions. Our adopted formula for t_{set} (Eq. 28) is designed to prevent this unphysical outcome.

Fig. 1c illustrates the ratios of dust-to-gas volume density ϵ and surface density Z . Due to dust trapping at the pressure bump, the disk metallicity Z gets largely elevated and exceeds 2–4%, whereas ϵ reaches the order of unity at the edge of the inner cavity as it sweeps outward.

We adopt the SI criterion from L24E (Eq. 21). In the end, planetesimals with a total mass of $31.4 M_{\oplus}$ are generated through this photoevaporation gas clearing process. The dust-to-planetesimal conversion efficiency is 20.4%, which indicates that 20.4% of the initial dust mass has been converted into planetesimals. The influences of alternative criteria of YG05 (Eq. 20) and L24Z (Eq. 22) on planetesimal formation are also tested. The total masses of resultant planetesimals show minor differences among all these criteria ($\lesssim 10\%$). Thus, the ϵ_{crit} criterion of L24E is used as the default in all following simulations.

Fig. 3a shows the evolution of the total dust mass (black line) and the planetesimal mass (red line) in `run_fid`. The blue bars represent the mass distribution of dust across different size bins within the pressure bump. The rapid rise of the planetesimal mass (red line) indicates that trapped dust particles are efficiently converted into planetesimals. This high formation efficiency results from the midplane volume density ratio ϵ being sufficiently high to trigger the SI at the cavity edge. Furthermore, after cavity

opening, the dust population within the pressure bump is predominantly composed of particles with Stokes numbers of 0.01–0.1. The contribution of the dust particles within the pressure bump to the final planetesimal mass depends solely on the mass fraction of the trapped dust particles.

To conclude, `run_fid` shows that stellar X-ray photoevaporation opens a cavity at a few au orbital distance. As the inner cavity sweeps inside-out, the dust particles accumulating at the cavity's edge can trigger the SI and form planetesimals efficiently. In total $30.5 M_{\oplus}$ of planetesimals are generated at $r=5\text{--}30$ au within 1 Myr after the onset of stellar X-ray photoevaporation.

3.2. Metallicity

We investigate the influence of disk metallicity on planetesimal formation, by increasing Z_0 from 0.01 in `run_fid` to 0.02 in `run_metal`. The other parameters are kept identical as `run_fid`.

Fig. 3b shows total dust mass and planetesimal mass in `run_metal`. The initial dust mass is $\sim 300 M_{\oplus}$, whereas $50 M_{\oplus}$ remains when the photoevaporation opens a cavity at $t=0.37$ Myr. For comparison, in `run_fid`, the initial dust mass is $\sim 150 M_{\oplus}$, whereas $37 M_{\oplus}$ remains at $t=0.37$ Myr (see Fig. 3a).

We find that `run_fid` yields a final planetesimal mass of $31.4 M_{\oplus}$, whereas in `run_metal` the final planetesimal mass reaches $48.2 M_{\oplus}$. Clearly, doubling the initial metallicity indeed results in an increase of the final planetesimal mass. But the final planetesimal mass in `run_metal` is not twice as high as in `run_fid`. This is because the dust in the `run_metal` experiences more rapid growth (see Eq. 12) compared to that in `run_fid`. In the early phase, the grown particles also get accreted by the central star at a faster rate. As a consequence, in both cases the masses of retained dust at the onset of photoevaporative cavity are overall similar.

3.3. Stellar X-ray luminosity

Meanwhile, we also test the effect of the stellar X-ray luminosity such that L_X is set to be $1.0 L_{X,\odot}$ in `run_lumi` rather than $2.6 L_{X,\odot}$ in `run_fid`. The other parameters are the same as `run_fid`.

Table 2 shows that `run_fid` yields a final planetesimal mass of $31.4 M_{\oplus}$ with an overall dust-to-planetesimal conversion effi-

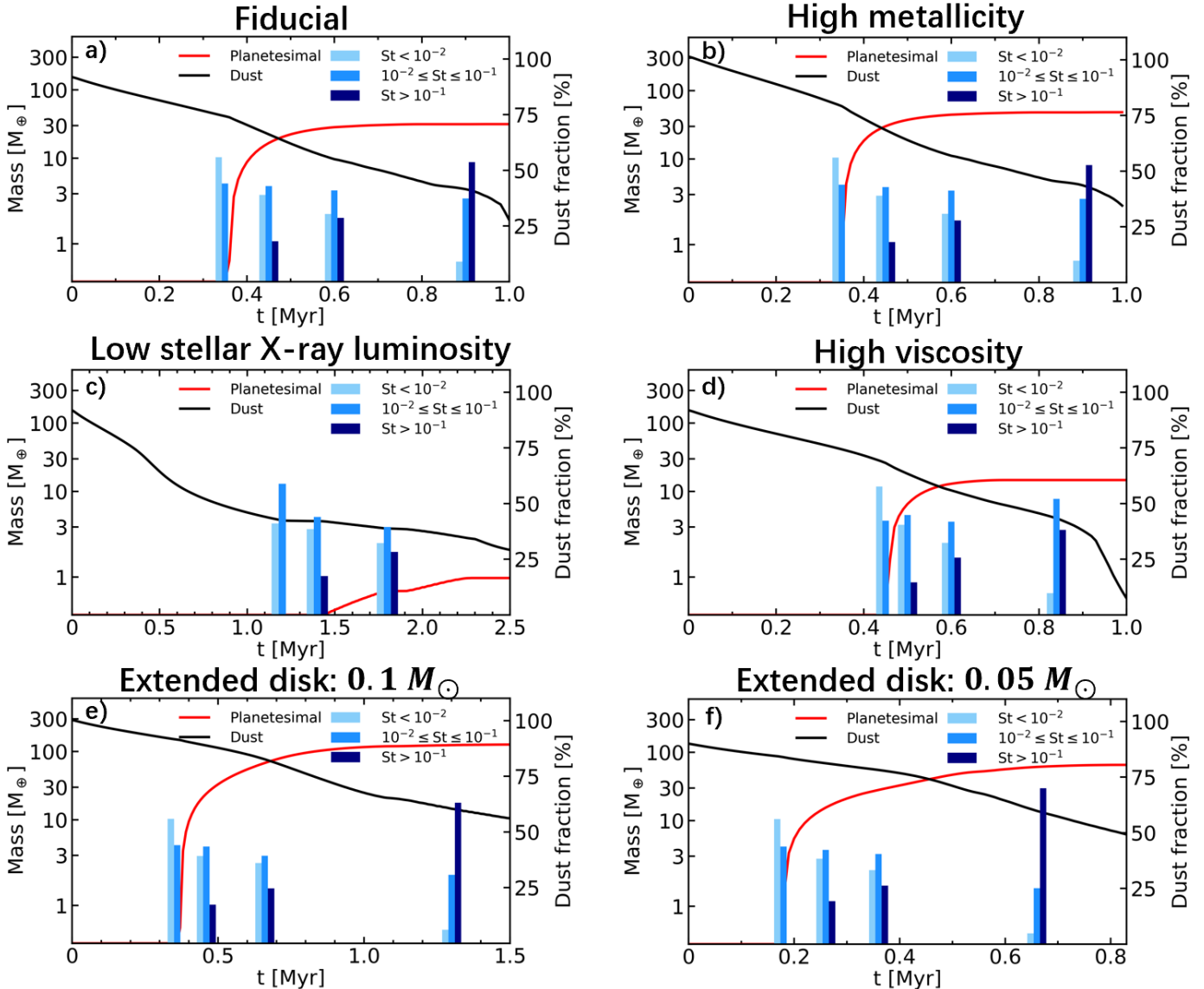


Fig. 3: The evolution of dust mass (black lines), planetesimal mass (red lines), and dust mass fraction within the pressure bump in three Stokes number bins (light-blue: $St < 10^{-2}$; blue: $10^{-2} \leq St \leq 10^{-1}$; deep-blue: $St > 10^{-1}$), across four evolutionary stages: (i) pre-cavity, (ii) cavity at 10 au, (iii) cavity at 20 au, and (iv) cavity at 100 au. These panels show how initial conditions affect dust retention and planetesimal formation: Panel a) Fiducial model ($Z = 0.01$, $L_X = 2.6 L_{X,\odot}$, $M_{\text{disk}} = 0.05 M_{\odot}$, $R_c = 60$ au, $\alpha = 10^{-4}$) serves as the baseline for comparison, showing balanced dust evolution and planetesimal production across the disk. Panel b) Higher metallicity ($Z = 0.02$) facilitates the retention of dust mass, thereby promoting planetesimal formation. Panel c) Decreased X-ray luminosity (from $2.6 L_{X,\odot}$ to $1.0 L_{X,\odot}$) diminishes dust mass, and consequently impedes planetesimal formation. Panel d) Higher viscosity parameters ($\alpha = 10^{-3}$, $\delta_t = 10^{-4}$) induce gas replenishment from the outer disk, delay cavity opening, reduce overall dust reservoir, and thus hinder planetesimal formation. Panel e) A more massive and extended disk ($M_{\text{disk}} = 0.1 M_{\odot}$, $R_c = 120$ au) prolongs dust retention, thereby extending the duration of planetesimal formation. Panel f) A less massive but extended disk ($M_{\text{disk}} = 0.05 M_{\odot}$, $R_c = 120$ au) lowers the inner-disk dust density, causing photoevaporation to open a cavity earlier. This makes more dust retained at the onset of photoevaporative cavity, which also provides more building blocks for planetesimal formation.

ciency of 20.4%, whereas `run_lumi` achieves a final planetesimal mass of only $1 M_{\oplus}$ with a low conversion efficiency of 0.6%. As can be seen from Fig. 3c, only $3.8 M_{\oplus}$ of dust is left when the photoevaporation opens a cavity at $t=1.2$ Myr in `run_lumi`.

The low stellar X-ray luminosity model results in a significant drop in the planetesimal mass and conversion efficiency. The strength of L_X is crucial to determine the time for the photoevaporation-driven cavity formation. The disk around a star with a low stellar X-ray luminosity results in the cavity-opening at a later time. By this time, a substantial amount of

dust has already been accreted to the star. As a consequence, only a limited amount of dust remains available for the planetesimal formation. Therefore, we suggest that a relatively high L_X is required to induce the generation of planetesimals at the gas clearing phase.

3.4. Viscosity

Disk viscosity, parameterized by α , drives the global evolution of the protoplanetary disk. We focus on isolating the role of viscos-

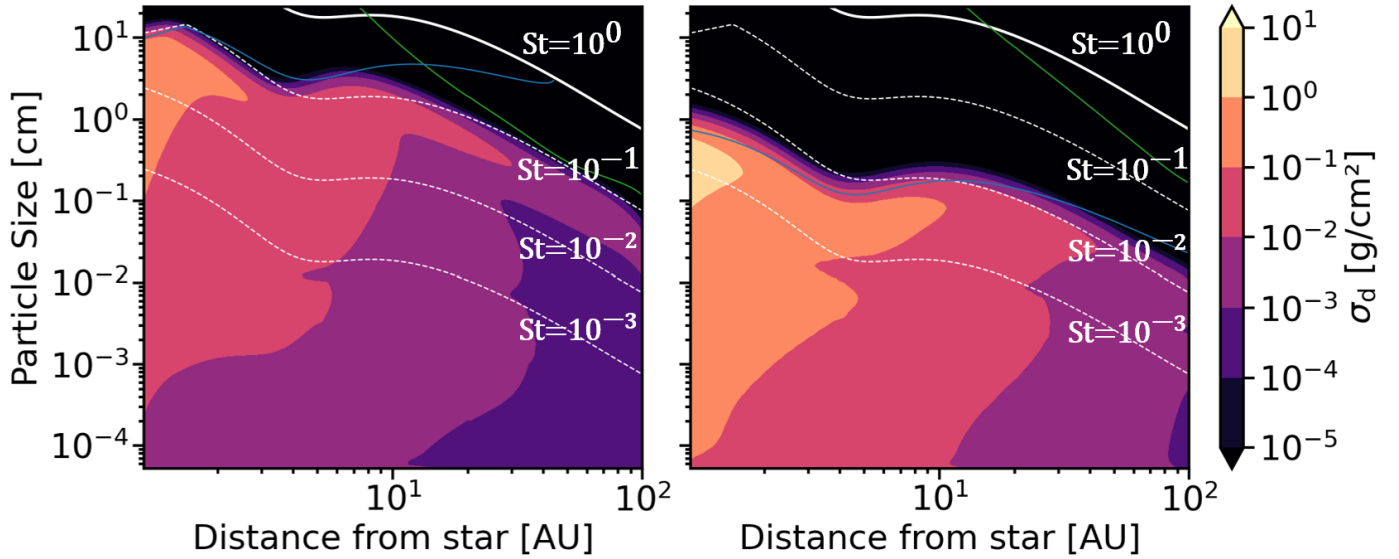


Fig. 4: The distribution of dust as a function of radial distance and particle size at $t=0.30$ Myr for `run_fid` (left) and `run_frag` (right). The color bar represents the surface density of dust per logarithmic mass interval. The green line is the drift limit (Eq. 14), whereas blue line is the fragmentation limit (Eq. 15). The four white lines correspond to $St=[10^{-3}, 10^{-2}, 10^{-1}, 10^0]$

ity α in global disk evolution and that of the turbulent parameter δ_t in dust coagulation. In other words, we treat α and δ_t differently. In `run_alpha` we only vary α from 10^{-4} to 10^{-3} whereas the turbulent mixing parameter δ_t is still kept the same. Thus, the particles' Stokes number set by the fragmentation limit is the same as in `run_fid`.

Fig. 3d reveals that at a high α of 10^{-3} , owing to more efficient angular momentum transport, the gas from the outer disk region replenishes the inner disk region at a fast pace. The cavity is opened at a later time of 0.45 Myr in `run_alpha`. As a result, a smaller amount of dust is left by this time and eventually lead to less planetesimal formation. Table 2 shows that the planetesimal mass decreases from $31.4 M_{\oplus}$ in `run_fid` to $14.6 M_{\oplus}$ in `run_alpha`.

3.5. Disk radius

The disk size is also a key factor that affects the gas/dust evolution and planetesimal formation. In `run_fid`, the characteristic disk radius R_c is set to be 60 au. Here we perform two additional sets of simulations to explore the influence of disk size. In `run_dsize1`, we keep Σ_{g0} at 1 au the same as that of `run_fid` and increase R_c to 120 au. In such a case the initial disk mass increases to $0.1 M_{\odot}$. On the other hand, in `run_dsize2`, the total disk mass is still kept the same as $0.05 M_{\odot}$ whereas R_c is increased to 120 au. This configuration leads to an overall lower Σ_{g0} in the inner disk region.

Fig. 3e & f depict the evolution of dust masses and planetesimal masses in these two cases. The disk is more massive and a higher proportion of dust mass resides in the outer disk region in `run_dsize1` compared to `run_fid`. Since the gas density remains approximately the same in the inner disk region for `run_fid` and `run_dsize1`, the photoevaporative cavity forms at a similar time. In `run_dsize1`, the residual dust mass reaches $\sim 144 M_{\oplus}$ at this cavity-opening time (see Fig. 3e). This leads to a higher planetesimal mass and conversion efficiency in the end.

On the other hand, `run_dsize2` refers to a circumstance that the gas mass is more readily distributed at further out disk

region. For `run_dsize2`, the gas density in the inner disk region is lower, and the photoevaporation opens a cavity at an earlier time of 0.18 Myr compared to `run_fid` (see Fig. 3f). This makes more dust retained at the onset of photoevaporative cavity, which also provides more building blocks for planetesimal formation.

As can be seen from Table 2, the conversion efficiencies in above two models are quite similar, but both much higher than `run_fid`. This again, indicates that regardless of the detailed treatment of Σ_g or M_{disk} , a disk with a larger size promotes the dust retention and thus subsequent planetesimal formation.

3.6. Dust fragmentation threshold velocity

In order to explore how the photoevaporation-driven planetesimal formation depends on the fragmentation-limited dust growth, we perform a simulation `run_frag` with a lower fragmentation threshold velocity of $v_{\text{frag}}=1 \text{ m s}^{-1}$. The other parameters are the same as `run_fid`.

Fig. 4 shows the distribution of dust as a function of radial distance and particle size at $t=0.30$ Myr for `run_fid` (left) and `run_frag` (right). It is evident that the particles' Stokes number in `run_fid` is more than one order of magnitude larger than that in `run_frag`. Because the growth is limited by fragmentation, the largest particles reach a lower Stokes number when the fragmentation threshold is lower. Such small particles are more strongly coupled to the disk gas, and hence drift more slowly. Consequently, they are less efficient to concentrate at the cavity's edge, preventing the SI clumping and subsequent planetesimal formation. As can be seen from Table 2, no planetesimal can form during the gas clearing phase in `run_frag`.

Lim et al. (2025b) and Lim et al. (2025a) conducted 2D and 3D simulations of pure SI without external turbulence, respectively. The SI criteria presented in these two studies suggested lower thresholds for the onset of the SI. However, it is worth noting that their simulations indicate that ϵ needs to exceed 2 to trigger the SI for particles with $St \leq 10^{-3}$. Hence, even adopting a loose SI criterion from Lim et al. (2025a) (their Eq. 11) with-

out considering any turbulence, planetesimals are still unlikely to form at a relatively low fragmentation velocity. Zhao et al. (2025) also concluded that $v_{\text{frag}}=2 \text{ m s}^{-1}$ was the minimum value that allowed planetesimal formation, which is consistent with our results.

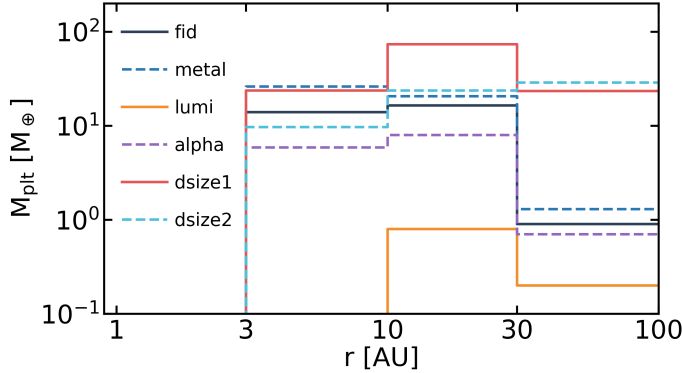


Fig. 5: Comparison of the radial mass distributions of planetesimals at different disk regions. The curves show the results for models with varying parameters: `run_fid` (black), `run_metal` (blue), `run_lumi` (orange), `run_alpha` (purple), `run_dsiz1` (red), and `run_dsiz2` (cyan).

To facilitate a direct comparison among different models, Fig. 5 presents the radial mass distributions of planetesimals. To conclude, our results indicate that planetesimal formation is more efficient in larger disks with higher metallicities, lower viscosities, higher dust fragmentation threshold velocities, and/or around stars with higher X-ray luminosities.

4. Discussions

We compare our work with the literature studies in Sect. 4.1. The influences of turbulent mixing parameters and pressure bumps produced by other mechanisms are presented in Sect. 4.2 and Sect. 4.3. Finally, the caveats in our model are discussed in Sect. 4.4.

4.1. Comparison with literature studies

We compare our results with those of Carrera et al. (2017) and Ercolano et al. (2017), who also explored planetesimal formation via the SI driven by the stellar X-ray photoevaporation.

First, our treatment of dust evolution differs from theirs. Whereas Carrera et al. (2017) used a custom 1D viscous disk code with simplified dust prescriptions from Birnstiel et al. (2011), and Ercolano et al. (2017) employed the two-population model of Birnstiel et al. (2012) in their 1D code, we utilize the open-source `DustPy` code, which incorporates full multi-size dust evolution, including coagulation, fragmentation, and radial drift. The other difference is the treatment of stellar X-ray photoevaporation. Carrera et al. (2017) adopted the model from Gorti et al. (2015), who considered FUV-driven disk dispersal. This process triggers strong radial pressure gradients and enhance the dust pile-ups in the early phase of the disk lifetime. Ercolano et al. (2017), by contrast, used both X-ray and EUV-driven photoevaporation prescription derived from Owen et al. (2010, 2012)'s hydrodynamic simulations. Consequently, in their works, disk gas was removed more gradually, and photoevaporation primarily affected the inner a few au region of the disk. While also adopting the stellar X-ray photo-

evaporation prescription from Owen et al. (2012), we additionally incorporate dust removal via photoevaporation, following the studies of Facchini et al. (2016) and Sellek et al. (2020).

There are two improvements in our study: the dust scale height calculation and SI criterion. Whereas the previous studies relied on simplified estimates for the midplane density, we implement the correction from Carrera et al. (2025) and Eriksson et al. (2025) (our Eq. 24), which self-consistently accounts for local turbulence and particle-size-dependent settling. This allows us to track dust evolution more precisely and significantly improves the accuracy of midplane density predictions. On the other hand, both Carrera et al. (2017) and Ercolano et al. (2017) adopted the classical threshold from the 2D unstratified simulations of Carrera et al. (2015). In this study, we instead adopt the latest criterion from Lim et al. (2024), which is based on 3D shearing box simulations and defines a critical midplane density ratio ϵ_{crit} . This criterion takes into account the external turbulence, reflecting a more realistic condition for dust-gas interaction in vertically stratified disks.

Regarding the planetesimal formation, Carrera et al. (2017) reported up to $60 M_{\oplus}$ of planetesimals formed beyond 100 au region, and $\sim 16 M_{\oplus}$ within 100 au. This high efficiency is a consequence of their adoption of strong FUV photoevaporation, which accelerates disk dispersal in the outer disk region and thus enhances dust concentration there. Conversely, Ercolano et al. (2017) found planetesimal formation is less likely for the X-ray and EUV photoevaporation. Their model produces only $3 M_{\oplus}$ under optimal conditions, due to rapid dust drift before gap formation and absence of strong pressure traps. Our results strike a middle ground. We demonstrate that stellar X-ray photoevaporation can still trigger localized SI when vertical dust settling is explicitly modeled. Because X-ray-driven winds have higher temperatures and thus smaller gravitational radii, the photoevaporative cavity opens at a smaller physical radius, allowing a larger fraction of solids to remain inside ~ 100 au and thereby promoting planetesimal formation within ~ 100 au. In our fiducial model, the total planetesimal mass can attain $30.5 M_{\oplus}$ within the 30 au disk region. By adopting a more realistic SI criterion and a sophisticated dust evolution treatment, our study indicates that stellar X-ray photoevaporation can also be robust for SI-triggered planetesimal formation.

4.2. Turbulent mixing parameters

Several turbulent-relevant parameters are used in this work: δ_r , δ_t and δ_z . Since disk turbulence can be non-isotropic, e.g., driven by the vertical shear instability (VSI) (Nelson et al. 2013) or non-ideal MHD (Yang et al. 2018), these parameters are not necessarily equal. As shown in Table 3, we conduct several simulations to investigate the influences of varying these parameters.

We perform a simulation `run_rad`, with considering the effect of turbulent radial diffusion on dust and other parameters kept identical as `run_fid`. The dust diffusion timescale in `run_rad` is given by

$$t_{\text{diff}} = \frac{(\Delta r)^2}{D_d} \simeq 1.5 \times 10^3 f^2 \left(\frac{\delta_r}{10^{-4}} \right)^{-1} \left(\frac{P_r}{1 \text{ yr}} \right) \text{ yr}, \quad (29)$$

where $\Delta r \sim f H_g$ is the pressure bump width at the onset of photoevaporation induced cavity, f is an order-unity factor, and P_r is the Keplerian period at the radial distance r .

Table 3: List of simulation setup, model parameters and resultant planetesimal masses in Sect. 4.2.

| Model | α | δ_r | δ_t | δ_z | v_{frag} [m s $^{-1}$] | M_{plt} [M_{\oplus}] |
|-----------|-----------|------------|------------|------------|----------------------------------|-----------------------------------|
| run_fid | 10^{-4} | 0 | 10^{-4} | 10^{-4} | 5 | 31.4 |
| run_alpha | 10^{-3} | 0 | 10^{-4} | 10^{-4} | 5 | 14.6 |
| run_rad | 10^{-4} | 10^{-4} | 10^{-4} | 10^{-4} | 5 | 30.9 |
| run_turb | 10^{-3} | 0 | 10^{-3} | 10^{-4} | 15 | 0.7 |
| run_vert | 10^{-4} | 0 | 10^{-4} | 10^{-6} | 5 | 20.9 |

The photoevaporative cavity expansion timescale can be estimated as

$$t_{\text{cav}} = \frac{\Delta r}{v_{\text{cav}}} = \frac{\Delta r}{r} \frac{\Sigma_{\text{cav}}}{\dot{\Sigma}_{\text{PE,g}}} \simeq 10^3 f^2 \left(\frac{\alpha}{10^{-4}} \right)^{-1} \left(\frac{P_r}{1 \text{ yr}} \right) \text{ yr}, \quad (30)$$

where $v_{\text{cav}} = r \dot{\Sigma}_{\text{PE,g}} / \Sigma_{\text{cav}}$ is the cavity expansion velocity, we emphasize that v_{cav} does not correspond to the physical radial velocity of the gas; rather, it represents the expansion speed (i.e., the phase velocity) of the photoevaporative cavity edge. $\Sigma_{\text{cav}} \simeq \dot{M}_{\text{acc}} / (3\pi\nu)$ denotes the critical gas surface density at which viscous accretion balances photoevaporative mass loss, and $\dot{M}_{\text{acc}} \simeq 2\pi r \Delta r \dot{\Sigma}_{\text{PE,g}}$ corresponds to the critical gas accretion rate.

We note that, in estimating t_{cav} , we have assumed $\dot{M}_{\text{acc}} \simeq 2\pi r \Delta r \dot{\Sigma}_{\text{PE,g}}$ for simplicity. In practice, however, the gas accretion rate after the onset of cavity opening is typically smaller than the photoevaporative mass-loss rate. This implies that our estimate of t_{cav} should be regarded as an upper limit. Therefore, we provide only an estimate that $t_{\text{cav}} \lesssim t_{\text{diff}}$. Although the exact reduction factor is difficult to quantify, this effect further reinforces our conclusion that radial diffusion cannot regulate the dust concentration at the cavity edge.

The dust particles settle and are subsequently converted into planetesimals on a timescale of

$$t_{\text{plt}} = \frac{1}{\zeta \text{St} \Omega_K} \simeq 16 \left(\frac{\zeta}{0.1} \right)^{-1} \left(\frac{\text{St}}{0.1} \right)^{-1} \left(\frac{P_r}{1 \text{ yr}} \right) \text{ yr}, \quad (31)$$

where St is the Stokes number of the maximum-size dust particles St (a_{max}), which follows St (a_{max}) $\simeq 0.1(r/\text{au})^{1/2}$ in the fiducial model.

It can be noted that, for the particles with Stokes numbers of 0.01–0.1, $t_{\text{plt}} \ll t_{\text{cav}} < t_{\text{diff}}$ in run_rad. Once the SI criterion is met, dust is converted into planetesimals on a timescale much shorter than both the outward expansion of the photoevaporative cavity edge and the radial dust diffusion timescale. In other words, planetesimal formation is completed before the cavity edge recedes and before diffusion can significantly redistribute the dust. Consequently, we find no substantial difference in the total planetesimal mass formed between run_rad and run_fid (see Table 3).

We set $\delta_r = 0$, since radial diffusion does not regulate the peak dust-to-gas ratio in the low δ_r and high L_X regime we focus on here. In this regime, photoevaporation drives the cavity edge outward on a timescale shorter than that required for radial dust diffusion to establish a local drift–diffusion equilibrium at the pressure maximum. More importantly, both t_{cav} and t_{diff} are much longer than t_{plt} . Once the SI is triggered, dust is rapidly converted into planetesimals, which naturally limits the peak dust-to-gas ratio.

Having explored the influence of the radial diffusion mechanism on planetesimal formation, we now turn our attention to another important parameter, δ_t . Furthermore, in order to investigate the influence of δ_t , we conduct a control simulation,

run_turb, based on run_alpha. As shown in Table 3, this control run maintains all other parameters the same as run_alpha, but adjusts δ_t to 10^{-3} and v_{frag} to 15 m s^{-1} . This ensures that the dust reach a similar Stokes number at the fragmentation limit in two simulations.

We can therefore isolate the effect of δ_t . Through this comparison, we find that an increase in δ_t leads to a reduction of final planetesimal mass (from $14.6 M_{\oplus}$ to $0.7 M_{\oplus}$). This phenomenon can be attributed to the fact that the relative velocity between particles increases with δ_t , and dust grows much faster in this circumstance (see Eq. 12). Consequently, the dust in the inner disk reaches the fragmentation limit at an earlier stage, leading to a less efficient retention of dust mass before the onset of photoevaporative cavity.

Similar to δ_t , δ_z also indirectly affects the planetesimal formation process by altering the dust growth timescale. We also establish a control simulation run_vert based on run_fid. As can be seen from Table 3, we reduce the value of δ_z from 10^{-4} in run_fid to 10^{-6} in run_vert. This reduction decreases the dust scale height, which both increases the midplane dust-to-gas and shortens the growth timescale. However, ϵ is not high enough to trigger the SI at early times, and fast growth leads rapid depletion of dust mass. In the end we find that less dust is retained by the time that cavity opens, leading to a decrease in the final planetesimal mass from $31.4 M_{\oplus}$ to $20.9 M_{\oplus}$.

4.3. Local pressure bump

Apart from the inner cavity generated by stellar X-ray photoevaporation, the pressure bumps associated with substructures can also be produced by other mechanisms, such as gap opening by massive planets (Kobayashi et al. 2012; Zhu et al. 2012; Gonzalez et al. 2015; Eriksson et al. 2020), at the inner edge of dead zones (Varnière & Tagger 2006; Lyra et al. 2009; Dzyurkevich et al. 2010), by zonal flows arising from hydrodynamic instabilities (Lehmann & Lin 2025) or magnetorotational turbulences (Johansen et al. 2009a), and in the ice line regions (Ida & Guillot 2016; Drążkowska & Alibert 2017; Schoonenberg & Ormel 2017). The pressure bumps act as traps that halt the inward drift and concentrate dust particles. Under favorable conditions, this process can trigger the SI and lead to planetesimal formation.

To further investigate the role of pressure bumps that may be produced by other mechanisms, we perform an additional simulation in which gaps are artificially imposed on the gas disk. The gap profile is adopted from Dullemond et al. (2018)

$$\alpha(r) = \alpha_0 / F(r), \quad (32)$$

where α_0 is the disk viscosity, and $F(r)$ is given by

$$F(r) = \exp \left[-A \exp \left(-(r - r_0)^2 / (2w^2) \right) \right], \quad (33)$$

where A is the gap amplitude, r_0 is the gap location, and w is the gap width.

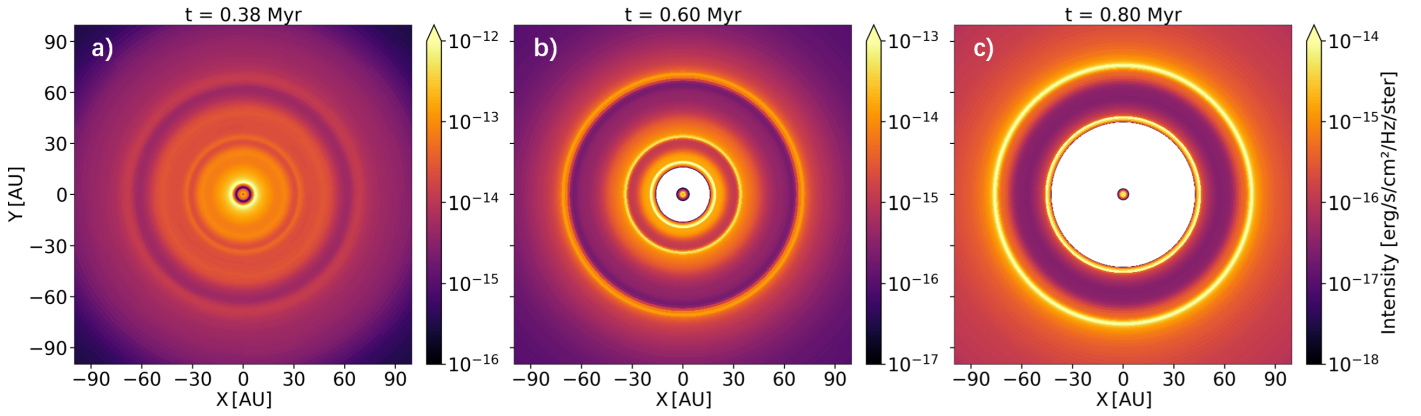


Fig. 6: Synthetic dust continuum images at $880 \mu\text{m}$ for three evolutionary stages of the protoplanetary disk model with three local pressure bumps at 30 au and 60 au in Sect. 4.3. Panel a): $t=0.38 \text{ Myr}$, pre-cavity stage; Panel b): $t=0.60 \text{ Myr}$, post-cavity stage when the photoevaporative cavity moves to 18 au ; Panel c): $t=0.80 \text{ Myr}$, when the photoevaporative cavity merges with the inner bump at 30 au . The blanks within the inner disks in Panel b) and c) correspond to the photoevaporative cavities.

Fig. 6 shows three snapshots of the dust continuum images at $880 \mu\text{m}$ with two artificial bumps at 30 au and 60 au , where $A=0.4$ and $w=0.1r_0$. Other parameters are the same as `run_fid`. At $t=0.38 \text{ Myr}$, the two wide gaps block the inward drifting of dust from the outer disk region before the onset of photoevaporative cavity (see Fig. 6a). We can see that the photoevaporative cavity forms and progressively moves outward. At $t=0.60 \text{ Myr}$ the cavity moves to 18 au (see Fig. 6b), whereas at $t=0.80 \text{ Myr}$ it merges with the inner bump at 30 au (see Fig. 6c).

The bumps can also be sites for dust trapping and planetesimal formation. Consequently, the total planetesimal mass increases from $31.4 M_\oplus$ to $33.9 M_\oplus$. Meanwhile, $\sim 7.6 M_\oplus$ mass of planetesimals form in the bumps, leading to a slight reduction in the planetesimal mass formed at the outer edge of the photoevaporative cavity, from $\sim 30.5 M_\oplus$ to $\sim 26.3 M_\oplus$. We also note that as photoevaporative cavity expands progressively outward, it merges with the existing bumps.

We compute the optical depth τ_ν following

$$\tau_\nu = \sum_i (\kappa_{\nu,i}^{\text{abs}} + \kappa_{\nu,i}^{\text{sca,eff}}) \Sigma_d^i, \quad (34)$$

where $\kappa_{\nu,i}^{\text{abs}}$ and $\kappa_{\nu,i}^{\text{sca,eff}} = (1 - g_{\nu,i}) \kappa_{\nu,i}^{\text{sca}}$ are the absorption and effective scattering opacities of dust species i , and Σ_d^i is the dust surface density of dust species i . The values of $\kappa_{\nu,i}^{\text{abs}}$, $\kappa_{\nu,i}^{\text{sca}}$ and $g_{\nu,i}$ are adopted from DSHARP opacity model (Birnstiel et al. 2018). The optical depth ($838 \mu\text{m}$) at the edge of photoevaporative cavity is ~ 2.1 at $t=0.60 \text{ Myr}$ (see Fig. A.1). The τ_ν values of the three bumps are approximately in the ratio of $4:2.4:1$, whereas the corresponding dust surface density ratios are $3:2:1$. The relatively high optical depth at the cavity edge arises not only from the larger dust surface density but also from the preferential removal of small particles by photoevaporation, which increases the fraction of particles larger than 1 mm . Since such large particles have higher opacities at the observation wavelength, the resulting τ_ν becomes significantly enhanced in this region.

Gárate et al. (2023) also studied the combined impact of early substructures and photoevaporation. They found that in disks with primordial substructures, once photoevaporation opened an inner cavity, further dust loss due to radial drift was largely prevented, and dust removal by wind entrainment had only a minor effect on the evolution of solids. Such disks can retain a substantial dust mass. The difference between their work

and ours is that they do not include the planetesimal formation. Furthermore, they indicated that the ratio of the gap location relative to the disk's characteristic radius r/R_c controls how much dust can be retained.

4.4. Caveats

We point out several limitations in our study. First, we neglect the interaction of dust onto gas, commonly referred to as dust-to-gas backreaction, in all of our simulations. This effect can be pronounced when the solid density approaches that of the surrounding gas ($\epsilon = \rho_d / \rho_g \sim 1$). From the classical SI perspective, the drag force exerted by dust particles accelerates the gas's azimuthal motion. This, in turn, suppresses the inward drift of solids and further increases the local dust-to-gas ratio, making planetesimal formation more favorable.

Nevertheless, near the pressure maximum of the photoevaporation cavity, this backreaction plays a dual role: whereas it slows down the drift of dust, the gas simultaneously gains angular momentum, which acts to widen the pressure bump. This broadening would on the other hand limit the further dust concentration. Consequently, the overall impact of backreaction on the SI and planetesimal formation can be more complicated. We also conduct an additional simulation based on `run_fid` that includes the dust-to-gas backreaction, implemented through the `DustPyLib` interface (Stammler et al. 2023). The result is overall similar in terms of final planetesimal mass, which decreases from $31.4 M_\oplus$ to $30.7 M_\oplus$.

The other limitation is not accounting for the effect of the ice line. Our model employs a static disk temperature profile and therefore does not account for the movement of the ice lines. Furthermore, we do not consider composition-dependent sublimation as pebbles drift across the ice lines of various species. The process of sublimation, followed by diffusion and re-condensation, could locally enhance the solid abundance near the ice line location (Ida & Guillot 2016; Drążkowska & Alibert 2017; Schoonenberg & Ormel 2017). Consequently, the omission of the above mechanisms likely leads to an underestimation of planetesimal formation near ice lines. Future models should incorporate an evolving disk thermal structure and track the compositional evolution of pebbles to properly model the influence of ice lines.

Here we also do not consider the bouncing barrier. Laboratory and numerical studies show that the bouncing barrier typically prevents further coagulation once the dust aggregates reach mm/cm in size (Zsom et al. 2010). Neglecting this effect may therefore overestimate the mass fraction of pebbles that can grow to the sizes relevant for triggering the SI.

Finally, we note that turbulence acts as a more complex role in realistic disk environments than that assumed in Lim et al. (2024). Large-scale structures developed from magnetorotational or hydrodynamic instabilities can create local pressure maxima that efficiently trap solids and promotes planetesimal formation. In particular, Eriksson et al. (2025) found that vortices can efficiently trap drifting dust at their pressure maxima, leading to locally enhanced dust-to-gas ratios. The weak turbulence and low relative velocities within the central regions of vortices facilitate particle growth, and once planetesimals form, they can continue to grow through efficient pebble accretion. Likewise, Carrera et al. (2025) identified a positive feedback between dust coagulation and the SI, where enhanced dust concentration reduces turbulence and drift, promoting further particle growth and a stronger SI. Moreover, Huang & Bai (2025) demonstrated that the interplay among the VSI, the RWI and the SI can produce strong dust clumping within vortices in the outer disk regions even at moderately low dust-to-gas ratios. These effects are not considered in our current work.

5. Conclusions

In this work, we employ the `DustPy` code to study the dust coagulation, fragmentation, and radial drift in a viscously accreting protoplanetary disk subject to stellar X-ray photoevaporation. Photoevaporation opens an inner cavity at a few au orbital distance, causing the disk's inner edge to expand radially outward as gas disperses. This process efficiently removes gas via photoevaporative winds, and therefore largely enhances the local dust-to-gas ratio at the pressure bump near the cavity's edge, which serves as a natural site to trigger the SI. We demonstrate that planetesimal formation via the SI, driven by the stellar X-ray photoevaporation, is robust during the disk dispersal phase. In our fiducial model, in total $31.4 M_{\oplus}$ of planetesimals form within the 100 au disk region. Furthermore, the exact choice of the SI criteria has little impact on the results.

We explore how the key physical processes regulate both the onset of the SI and the final masses of planetesimals. We find that the efficiency of SI-induced planetesimal formation is strongly regulated by the available dust reservoir and its retention during disk evolution. Higher metallicity retains dust mass more effectively, directly enhancing planetesimal formation. Higher viscosity induces faster gas replenishment from the outer disk region, delays cavity opening, reduces overall dust reservoir, and thus hinders planetesimal formation. Higher stellar X-ray luminosity promotes earlier photoevaporative cavity opening while preserving dust at the cavity edge, thereby favoring planetesimal formation. Larger disks prolong dust retention, thereby extending the duration of planetesimal formation. By retaining dust more efficiently, substructured disks create favorable conditions for planetesimal formation. To summarize, our models suggest that planetesimal formation is favored in disks with larger sizes, substructures, higher metallicities, lower viscosities, higher dust fragmentation threshold velocities, and/or around stars with higher X-ray luminosities.

Future work will focus on the growth and migration of these forming planetesimals (Fang et al. 2023; Lau et al. 2022,

2024, 2025) starting from a realistic birth mass distribution (Schäfer et al. 2017; Liu et al. 2020).

References

Alexander, R., Pascucci, I., Andrews, S., Armitage, P., & Cieza, L. 2014, *Protostars and Planets VI*, 475

Andrews, S. M. 2020, *ARA&A*, 58, 483

Bai, X.-N. 2014, *ApJ*, 791, 137

Bai, X.-N. & Stone, J. M. 2010, *ApJ*, 722, 1437

Batalha, N. M., Rowe, J. F., Bryson, S. T., et al. 2013, *ApJS*, 204, 24

Birnstiel, T., Dullemond, C. P., Zhu, Z., et al. 2018, *ApJL*, 869, L45

Birnstiel, T., Fang, M., & Johansen, A. 2016, *Space Science Reviews*, 205, 41

Birnstiel, T., Klahr, H., & Ercolano, B. 2012, *A&A*, 539, A148

Birnstiel, T., Ormel, C., & Dullemond, C. 2011, *A&A*, 525, A11

Bitsch, B., Lambrechts, M., & Johansen, A. 2015, *A&A*, 582, A112

Blum, J. & Münch, M. 1993, *Icarus*, 106, 151

Blum, J. & Wurm, G. 2000, *Icarus*, 143, 138

Blum, J. & Wurm, G. 2008, *ARA&A*, 46, 21

Booth, R. A. & Clarke, C. J. 2021, *MNRAS*, 502, 1569

Brauer, F., Dullemond, C., & Henning, T. 2008, *A&A*, 480, 859

Burn, R., Emsenhuber, A., Weder, J., et al. 2022, *A&A*, 666, A73

Carrera, D., Gorti, U., Johansen, A., & Davies, M. B. 2017, *ApJ*, 839, 16

Carrera, D., Johansen, A., & Davies, M. B. 2015, *A&A*, 579, A43

Carrera, D., Lim, J., Eriksson, L. E., Lyra, W., & Simon, J. B. 2025, *A&A*, 696, L23

Cassan, A., Kubas, D., Beaulieu, J.-P., et al. 2012, *Nature*, 481, 167

Clarke, C. & Pringle, J. 1988, *MNRAS*, 235, 365

Dittrich, K., Klahr, H., & Johansen, A. 2013, *ApJ*, 763, 117

Dominik, C. & Tielens, A. 1997, *ApJ*, 480, 647

Drażkowska, J. & Alibert, Y. 2017, *A&A*, 608, A92

Drażkowska, J., Alibert, Y., & Moore, B. 2016, *A&A*, 594, A105

Drażkowska, J., Bitsch, B., Lambrechts, M., et al. 2023, *Protostars and Planets VII*, 534, 717

Drażkowska, J., Windmark, F., & Dullemond, C. P. 2014, *A&A*, 567, A38

Dubrulle, B., Morfill, G., & Sterzik, M. 1995, *Icarus*, 114, 237

Dullemond, C. P., Birnstiel, T., Huang, J., et al. 2018, *ApJL*, 869, L46

Dzyurkevich, N., Flock, M., Turner, N. J., Klahr, H., & Henning, T. 2010, *A&A*, 515, A70

Emsenhuber, A., Mordasini, C., Burn, R., et al. 2021, *A&A*, 656, A69

Ercolano, B., Jennings, J., Rosotti, G., & Birnstiel, T. 2017, *MNRAS*, 472, 4117

Ercolano, B. & Pascucci, I. 2017, *Royal Society Open Science*, 4, 170114

Eriksson, L. E., Johansen, A., & Liu, B. 2020, *A&A*, 635, A110

Eriksson, L. E. J., Menon, S., Carrera, D., Lyra, W., & Burkhardt, B. 2025, *MNRAS*, 542, 641

Facchini, S., Clarke, C. J., & Bisbas, T. G. 2016, *MNRAS*, 457, 3593

Fang, T., Zhang, H., Liu, S., Liu, B., & Deng, H. 2023, *ApJ*, 948, 98

Gárate, M., Birnstiel, T., Pinilla, P., et al. 2023, *A&A*, 679, A15

Gárate, M., Delage, T. N., Stadler, J., et al. 2021, *A&A*, 655, A18

Gonzalez, J.-F., Laibe, G., Maddison, S., Pinte, C., & Ménard, F. 2015, *Planetary and Space Science*, 116, 48

Gorti, U., Hollenbach, D., & Dullemond, C. 2015, *ApJ*, 804, 29

Güttler, C., Blum, J., Zsom, A., Ormel, C. W., & Dullemond, C. P. 2010, *A&A*, 513, A56

Huang, J., Andrews, S. M., Dullemond, C. P., et al. 2018, *ApJL*, 869, L42

Huang, P. & Bai, X.-N. 2025, *ApJL*, 986, L13

Ida, S. & Guillot, T. 2016, *A&A*, 596, L3

Ida, S. & Lin, D. N. 2004, *ApJ*, 604, 388

Jennings, J., Ercolano, B., & Rosotti, G. P. 2018, *MNRAS*, 477, 4131

Johansen, A., Blum, J., Tanaka, H., et al. 2014, *Protostars and Planets VI*, 547

Johansen, A. & Klahr, H. 2005, *ApJ*, 634, 1353

Johansen, A., Oishi, J. S., Low, M.-M. M., et al. 2007, *Nature*, 448, 1022

Johansen, A., Youdin, A., & Klahr, H. 2009a, *ApJ*, 697, 1269

Johansen, A., Youdin, A., & Mac Low, M.-M. 2009b, *ApJ*, 704, L75

Kataoka, A., Tanaka, H., Okuzumi, S., & Wada, K. 2013, *A&A*, 557, L4

Kobayashi, H., Ormel, C., & Ida, S. 2012, in *AAS/Division for Planetary Sciences Meeting Abstracts# 44*, Vol. 44, 415–11

Lau, T. C. H., Birnstiel, T., Drążkowska, J., & Stammler, S. M. 2024, *A&A*, 688, A22

Lau, T. C. H., Birnstiel, T., Stammler, S. M., & Drążkowska, J. 2025, *ApJ*, 994, 74

Lau, T. C. H., Drążkowska, J., Stammler, S. M., Birnstiel, T., & Dullemond, C. P. 2022, *A&A*, 668, A170

Lehmann, M. & Lin, M.-K. 2025, *ApJ*, 983, 135

Li, R. & Youdin, A. N. 2021, *ApJ*, 919, 107

Lim, J., Simon, J. B., Li, R., et al. 2024, *ApJ*, 969, 130

Lim, J., Simon, J. B., Li, R., et al. 2025a, *arXiv preprint arXiv:2509.18270*

Lim, J., Simon, J. B., Li, R., et al. 2025b, *ApJ*, 981, 160

Lissauer, J. J. 1993, *ARA&A*, 31, 129

Liu, B. & Ji, J. 2020, RAA, 20, 164

Liu, B., Lambrechts, M., Johansen, A., & Liu, F. 2019, A&A, 632, A7

Liu, B., Lambrechts, M., Johansen, A., Pascucci, I., & Henning, T. 2020, A&A, 638, A88

Lynden-Bell, D. & Pringle, J. E. 1974, MNRAS, 168, 603

Lyra, W., Johansen, A., Zsom, A., Klahr, H., & Piskunov, N. 2009, A&A, 497, 869

Mayor, M. 2011, A&A

Miller, E., Marino, S., Stammmer, S., et al. 2021, MNRAS, 508, 5638

Mordasini, C., Alibert, Y., Klahr, H., & Henning, T. 2012, A&A, 547, A111

Mulders, G. D., Pascucci, I., Apai, D., & Ciesla, F. J. 2018, AJ, 156, 24

Nakagawa, Y., Sekiya, M., & Hayashi, C. 1986, Icarus, 67, 375

Nelson, R. P., Gressel, O., & Umurhan, O. M. 2013, MNRAS, 435, 2610

Okuzumi, S., Tanaka, H., Kobayashi, H., & Wada, K. 2012, ApJ, 752, 106

Ormel, C. & Cuzzi, J. 2007, A&A, 466, 413

Owen, J., Ercolano, B., Clarke, C., & Alexander, R. 2010, MNRAS, 401, 1415

Owen, J. E., Clarke, C. J., & Ercolano, B. 2012, MNRAS, 422, 1880

Pan, M., Liu, B., Jiang, L., et al. 2025, ApJ, 985, 7

Picogna, G., Ercolano, B., Owen, J. E., & Weber, M. L. 2019, MNRAS, 487, 691

Pinilla, P., Birnstiel, T., Ricci, L., et al. 2012, A&A, 538, A114

Pinilla, P., Tazzari, M., Pascucci, I., et al. 2018, ApJ, 859, 32

Pollack, J. B., Hubickyj, O., Bodenheimer, P., et al. 1996, Icarus, 124, 62

Preibisch, T., Kim, Y.-C., Favata, F., et al. 2005, ApJS, 160, 401

Raettig, N., Klahr, H., & Lyra, W. 2015, ApJ, 804, 35

Safronov, V. S. 1972, in Evolution of the protoplanetary cloud and formation of the earth and the planets, ed. V. S. Safronov (Moscow: Nauka. Transl. 1972 NASA Tech. F-677)

Schäfer, U., Yang, C.-C., & Johansen, A. 2017, A&A, 597, A69

Schoonenberg, D. & Ormel, C. W. 2017, A&A, 602, A21

Schoonenberg, D., Ormel, C. W., & Krijt, S. 2018, A&A, 620, A134

Sekiya, M. & Onishi, I. K. 2018, ApJ, 860, 140

Sellek, A. D., Booth, R. A., & Clarke, C. J. 2020, MNRAS, 492, 1279

Sellek, A. D., Grassi, T., Picogna, G., et al. 2024, A&A, 690, A296

Shakura, N. I. & Sunyaev, R. A. 1973, Astronomy and Astrophysics, Vol. 24, p. 337-355, 24, 337

Simon, J. B., Armitage, P. J., Li, R., & Youdin, A. N. 2016, ApJ, 822, 55

Smoluchowski, M. v. 1916, Zeitschrift für Physik, 17, 557

Stammmer, S. M. & Birnstiel, T. 2022, ApJ, 935, 35

Stammmer, S. M., Birnstiel, T., & Gárate, M. 2023, Astrophysics Source Code Library, ascl

Stammmer, S. M., Drażkowska, J., Birnstiel, T., et al. 2019, ApJL, 884, L5

Throop, H. B. & Bally, J. 2005, ApJ, 623, L149

Varnière, P. & Tagger, M. 2006, A&A, 446, L13

Wang, L. & Goodman, J. J. 2017, ApJ, 835, 59

Weidenschilling, S. 1977, MNRAS, 180, 57

Weidenschilling, S. 1980, Icarus, 44, 172

Whipple, F. 1973, NASA, Washington Evolutionary and Phys. Properties of Meteoroids

Whipple, F. L. 1972, in From plasma to planet, 211

Xu, Z. & Bai, X.-N. 2022, ApJL, 937, L4

Yang, C.-C., Johansen, A., & Carrera, D. 2017, A&A, 606, A80

Yang, C.-C., Mac Low, M.-M., & Johansen, A. 2018, ApJ, 868, 27

Youdin, A. N. & Goodman, J. 2005, ApJ, 620, 459

Youdin, A. N. & Lithwick, Y. 2007, Icarus, 192, 588

Zhao, H., Lau, T. C. H., Birnstiel, T., Stammmer, S. M., & Drażkowska, J. 2025, A&A, 694, A205

Zhou, T., Deng, H.-P., Chen, Y.-X., & Lin, D. N. C. 2022, ApJ, 940, 117

Zhu, W. & Dong, S. 2021, ARAA, 59, 291

Zhu, Z., Nelson, R. P., Dong, R., Espaillat, C., & Hartmann, L. 2012, ApJ, 755, 6

Zhu, Z. & Yang, C.-C. 2021, MNRAS, 501, 467

Zsom, A., Ormel, C. W., Güttler, C., Blum, J., & Dullemond, C. 2010, A&A, 513, A57

Appendix A: Optical depth

We compute the optical depth τ_ν following

$$\tau_\nu = \sum_i (\kappa_{\nu,i}^{\text{abs}} + \kappa_{\nu,i}^{\text{sca,eff}}) \Sigma_d^i, \quad (\text{A.1})$$

where $\kappa_{\nu,i}^{\text{abs}}$ and $\kappa_{\nu,i}^{\text{sca,eff}} = (1 - g_{\nu,i}) \kappa_{\nu,i}^{\text{sca}}$ are the absorption and effective scattering opacities of dust species i , and Σ_d^i is the dust surface density of dust species i . The values of $\kappa_{\nu,i}^{\text{abs}}$, $\kappa_{\nu,i}^{\text{sca}}$ and $g_{\nu,i}$ are adopted from DSHARP opacity model (Birnstiel et al. 2018).

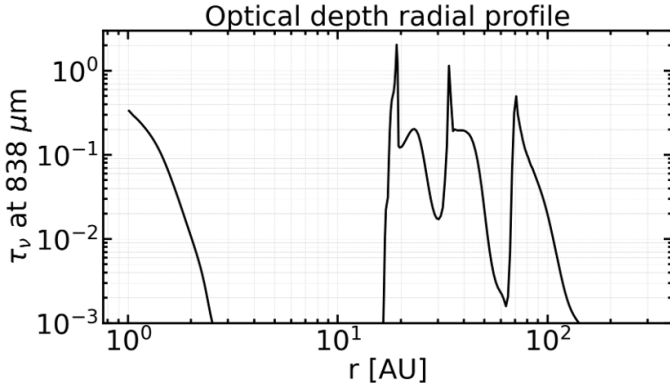


Fig. A.1: Radial profiles of the optical depth τ_ν at $838 \mu\text{m}$ for the three pressure bumps at $t=0.60 \text{ Myr}$.

The optical depth ($838 \mu\text{m}$) at the edge of photoevaporative cavity is ~ 2.1 at $t=0.60 \text{ Myr}$. The τ_ν values of the other two bumps are approximately ~ 1.2 at $\sim 34 \text{ au}$ and ~ 0.5 at $\sim 70 \text{ au}$. The optical depth of the outer bump at $\sim 70 \text{ au}$ is consistent with the results reported by Dullemond et al. (2018), who showed that observed outer disk rings typically have optical depths of order ~ 0.5 . Stammer et al. (2019) attributed these moderate optical depths to ongoing planetesimal formation, in agreement with our findings. In contrast, our results indicate significantly higher optical depths at the photoevaporative cavity edge and in the inner bump.

Appendix B: Dust entrainment

In this work, we adopt the dust entrainment model of Sellek et al. (2020) as our fiducial prescription for dust removal by photoevaporation. However, subsequent studies by Booth & Clarke (2021) and Burn et al. (2022) suggested that the entrained dust size may be significantly smaller, motivating an alternative dust entrainment model driven by internal photoevaporation.

$$a_{\text{ent,int}} = \sqrt{\frac{8}{\pi} \frac{\dot{\Sigma}_{\text{PE,g}}}{\rho_\bullet \Omega_K} \frac{H_{\text{base}}}{z_{\text{base}}} \left(1 + \frac{z_{\text{base}}^2}{r^2}\right)^{3/2}}, \quad (\text{B.1})$$

where $H_{\text{base}} \approx H_g$ denotes the gas scale height at the wind base, and z_{base} is the height at which the photoevaporative wind is launched. We adopt $z_{\text{base}}/H_{\text{base}} = 4$ as suggested by Booth & Clarke (2021). The maximum entrained size $a_{\text{ent,int}}$ is limited to only a few microns.

To assess the impact of these different assumptions, we perform a set of comparative simulations using three models: the fiducial model (FID), the pure gas photoevaporation model (PG), and the dust entrainment model driven by internal photoevaporation (IDE). Fig. B.1 shows the time evolution of the total planetesimal mass M_{plt} for the three models, whereas Fig. B.2

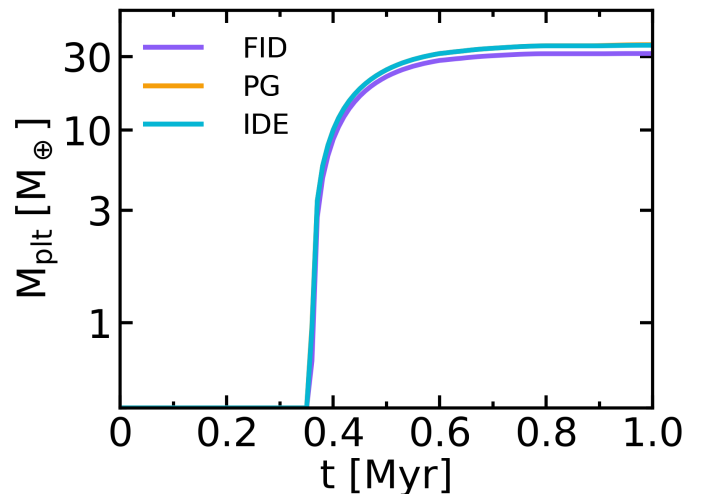


Fig. B.1: Time evolution of the planetesimal mass M_{plt} for three models FID, PG and IDE.

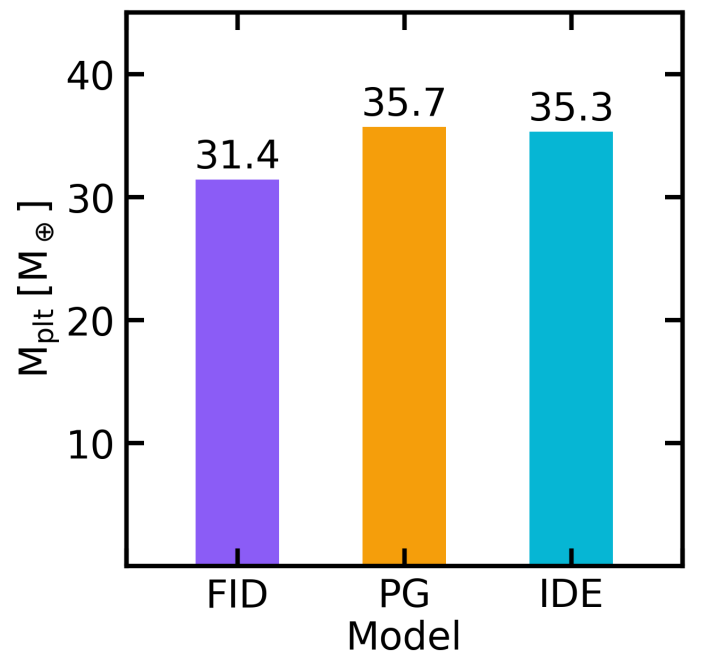


Fig. B.2: Total planetesimal mass M_{plt} for three models FID, PG and IDE.

compares the final planetesimal mass obtained at the end of the simulations.

We find that there is no significant difference between the PG and IDE models, either in the time evolution of M_{plt} or in the final planetesimal mass. This similarity arises because, in the IDE model, only dust particles with sizes of a few microns are efficiently entrained by the photoevaporative winds, leaving the bulk of dust mass largely unaffected. In contrast, the FID model, which allows the removal of larger dust particles, systematically underestimates the final planetesimal mass. We will improve the treatment of dust entrainment in future work.